A high-order multiscale discontinuous Galerkin method for the one-dimensional stationary Schrödinger equation

Bo Dong*and Wei Wang†

Abstract

In this paper, we extend our previous work on the second-order multiscale discontinuous Galerkin (DG) method for one-dimensional stationary Schrödinger equations with oscillating solutions [10] to high order. We propose two types of high-order multiscale finite element spaces, and prove that the resulting DG methods with these spaces converge optimally with respect to the mesh size h in L^2 norm when h is small enough. Numerically we observe that these two multiscale DG methods achieve at least the second-order convergence without any resonance errors when $h \gtrsim \varepsilon$ and optimal high-order convergence when $h \lesssim \varepsilon$, where ε is the scale of the wave length. We also demonstrate their ability to capture highly oscillating solutions of the Schrödinger equation in the application of the resonant tunneling diode (RTD) model.

Key words: high order, discontinuous Galerkin method, multiscale method, Schrödinger equation

1 Introduction

We propose, analyze, and numerically test two high-order multiscale discontinuous Galerkin (DG) methods for the following one-dimensional second-

*Email: bdong@umassd.edu. Department of Mathematics, University of Massachusetts Dartmouth, North Dartmouth, MA 02747.

†E-mail: weiwang1@fiu.edu. Department of Mathematics & Statistics, Florida International University, Miami, FL, 33199.

order equation

$$-\varepsilon^2 u'' - f(x)u = 0, \tag{1.1}$$

where $\varepsilon > 0$ is a small parameter and $f(x)$ is a real-valued smooth function. This type of equation has the application to the stationary Schrödinger equation in the modeling of quantum transport in nanoscale semiconductors [5, 14, 18],

$$\begin{cases} -\frac{\hbar^2}{2m}\varphi''(x) - qV(x)\varphi(x) = E\varphi(x) \quad \text{on } [a,b] \\ \hbar\varphi'(a) + \boldsymbol{i}p(a)\varphi_p(a) = 2\boldsymbol{i}p(a), \quad \hbar\varphi_p'(b) = \boldsymbol{i}p(b)\varphi(b), \end{cases} \tag{1.2}$$

where $\hbar$ is the reduced Plank constant, m is the effective mass (assumed to be constant), q is the elementary positive charge of the electron, $V(x)$ is the total electrostatic potential in the device, E is the injection energy, $p(x) = \sqrt{2m(E+qV(x))}$ is the momentum, and the solution φ is a wave function. By defining $\varepsilon = \dfrac{\hbar}{\sqrt{2mE}}$ and $f(x) = 1 + \dfrac{qV(x)}{E}$, the Schrödinger equation (1.2) is in the form of model equation (1.1).

The solution to the model equation (1.1) for positive f is a wave function with the wave length at the scale of ε. When ε is very small, the solution to this equation will be highly oscillating. Standard numerical methods require very fine meshes to resolve such oscillations, which leads to tremendous computational cost. So it is an important, yet formidable task to develop efficient multiscale numerical methods that produce accurate approximations to the solutions on coarse meshes. Note that when $f < 0$, the solution is non-oscillatory. Thus we mainly focus on the challenging case of $f(x) \geq \tau > 0$ and $0 < \varepsilon \ll 1$.

This paper contributes to an ongoing effort to develop multiscale methods for efficiently solving stationary Schrödinger equations with highly oscillatory solutions on coarse meshes; see [15, 16, 5, 4, 14, 18, 3]. In [5], Ben Abdallah and Pinaud proposed a second-order multiscale continuous finite element method for the one-dimensional Schrödinger equation with continuous WKB basis functions from WKB asymptotics [6]. The method was proved to have the second-order convergence independent of the wave length in [14]. However, it is difficult to extend the method to higher order or multiple dimensions due to the challenge of enforcing continuity of the non-polynomial finite element functions across inter-element faces. Unlike continuous finite element methods, DG methods [2, 9, 8] do not enforce continuity at element interfaces, which makes them feasible to be extended

to high-order approximations. Multiscale DG methods with non-polynomial basis functions have been developed and studied in the literature, including [1, 19, 12, 20, 7, 13, 18, 17, 21]. In particular, in [18] Wang and Shu adopted the DG framework and developed a multiscale local DG method using the "constant form" of WKB basis functions. Recently, in [10] we developed and analyzed a second-order multiscale DG method for Eq. (1.1), and showed that the method uses a smaller finite element space than the multiscale local DG method in [18] while achieving the same second order of accuracy with no resonance errors when $h \gtrsim \varepsilon$.

In this paper, we extend the second-order multiscale DG method in [10] to higher-order methods. The methods use the same weak formulation and numerical fluxes as in [10], but with higher-order multiscale finite element spaces. In particular, we consider two types of multiscale finite element spaces, both of which are extensions of the E^1 multiscale finite element space used in [10]. The first type of space is obtained by enriching the E^1 space with polynomial functions and the second one is by including more exponential functions into the E^1 space. Theoretically we prove that the multiscale DG methods on these two spaces both converge optimally with respect to the mesh size h in L^2 norm when h is small enough. This is obtained by proving the trace inequality and the approximation properties of the L^2 projections for the two multiscale finite element spaces, together with the energy and duality arguments used in [10]. Numerically we observe that these two methods can achieve at least the second-order convergence without any resonance errors when $h \gtrsim \varepsilon$ and an optimal high-order convergence when $h \lesssim \varepsilon$. Thus, these high-order multiscale DG methods behave like "hybrid" schemes where they perform as good as the second-order multiscale DG with E^1 when $h \gtrsim \varepsilon$ and as good as (in fact better than) standard DG with polynomial basis when $h \lesssim \varepsilon$. It is especially useful when applying these schemes to the multiscale problems with different scales of ε because they can capture the micro-scale solutions well in under-resolved mesh and also can maintain high order accuracy for macro scales.

The paper is organized as follows. In Section 2, we define our multiscale DG methods with the proposed high-order finite element spaces. In Section 3, we state and prove the error estimates. Numerical results are shown in Section 4. Finally, we conclude in Section 5.

2 Multiscale DG method: The Methodology

2.1 The DG formulation

The model problem we investigate in this paper is the equation (1.1) together with open boundary conditions, which is as follows:

$$\begin{cases} -\varepsilon^2 u'' - f(x)u = 0, \quad x \in [a,b], \\ u'(a) + \boldsymbol{i}k(a)\,u(a) = 2\boldsymbol{i}k(a), \quad u'(b) - \boldsymbol{i}k(b)\,u(b) = 0, \end{cases} \tag{2.1}$$

where $k(x) = \dfrac{\sqrt{f(x)}}{\varepsilon}$ is the wave number.

First we rewrite the problem (2.1) into a system of first order equations

$$q - \varepsilon u' = 0, \quad -\varepsilon q' - f(x)u = 0 \tag{2.2a}$$

with the boundary conditions

$$q(a) + \boldsymbol{i}\sqrt{f_a}\,u(a) = 2\boldsymbol{i}\sqrt{f_a}, \quad q(b) - \boldsymbol{i}\sqrt{f_b}\,u(b) = 0, \tag{2.2b}$$

where $f_a = f(a)$ and $f_b = f(b)$.

Let $I_j = (x_{j-\frac{1}{2}}, x_{j+\frac{1}{2}}), j = 1, \ldots, N$, be a partition of the domain, $x_j = \frac{1}{2}(x_{j-\frac{1}{2}} + x_{j+\frac{1}{2}})$, $h_j = x_{j+\frac{1}{2}} - x_{j-\frac{1}{2}}$, and $h = \max\limits_{j=1,\cdots,N} h_j$. Let $\Omega_h := \{I_j : j = 1, \ldots, N\}$ be the collection of all elements, $\partial\Omega_h := \{\partial I_j : j = 1, \ldots, N\}$ be the collection of the boundaries of all elements, $\mathscr{E}_h := \{x_{j+\frac{1}{2}}\}_{j=0}^{N}$ be the collection of all the element interfaces, and $\mathscr{E}_h^i := \{x_{j+\frac{1}{2}}\}_{j=1}^{N-1}$ be the collection of all interior element interfaces.

Next, to define our multiscale DG methods, we need to introduce the finite element spaces and the weak formulation of the approximate solutions, as well as the numerical traces that appear in the weak formulation.

Unlike standard DG methods using discontinuous piecewise polynomials for approximations, our multiscale DG methods look for approximate solutions in finite element spaces that contain non-polynomial functions. These functions are globally discontinuous and they incorporate the small scales of the problem so as to better approximate the oscillating solutions on coarse meshes. We will discuss our multiscale finite element spaces in detail in Section 2.2.

The weak formulation of our DG methods for Equation (2.2a) is to find approximate solutions u_h and q_h in a finite element space V_h such that

$$(q_h, w)_{\Omega_h} + (\varepsilon u_h, w')_{\Omega_h} - \langle \varepsilon \widehat{u}_h, w\,\boldsymbol{n}\rangle_{\partial\Omega_h} = 0 \tag{2.3a}$$

$$(\varepsilon q_h, v')_{\Omega_h} - \langle \varepsilon \widehat{q}_h, v\,\boldsymbol{n}\rangle_{\partial\Omega_h} - (f(x)u_h, v)_{\Omega_h} = 0. \tag{2.3b}$$

for all test functions $v_h, w_h \in V_h$. Here, we have used the notation

$$\begin{aligned}
(\varphi, v)_{I_j} =& \int_{I_j} \varphi(x)\overline{v}(x)\,dx,\\
\langle \psi, w\,\boldsymbol{n}\rangle_{\partial I_j} =& \psi(x_{j+\frac{1}{2}})\overline{w}(x_{j+\frac{1}{2}}) - \psi(x_{j-\frac{1}{2}})\overline{w}(x_{j-\frac{1}{2}}),\\
(\varphi, v)_{\Omega_h} =& \sum_{j=1}^{N}(\varphi, v)_{I_j}, \quad \langle \psi, w\,\boldsymbol{n}\rangle_{\partial\Omega_h} = \sum_{j=1}^{N}\langle \psi, w\,\boldsymbol{n}\rangle_{\partial I_j},
\end{aligned}$$

where $\overline{v}$ is the complex conjugate of v and $\boldsymbol{n}$ is the unit outward normal vector. For $I_j = (x_{j-\frac{1}{2}}, x_{j+\frac{1}{2}})$, we assume $\boldsymbol{n}(x_{j-\frac{1}{2}}) = -1$ and $\boldsymbol{n}(x_{j+\frac{1}{2}}) = 1$.

The choices of numerical traces are essential for the definition of DG methods, and different numerical traces will lead to different DG methods [2]. In our schemes, we use the same numerical traces as in our previous work [10]. At the interior element interfaces,

$$\widehat{u}_h(x_{j+\frac{1}{2}}) = u_h^-(x_{j+\frac{1}{2}}) - \boldsymbol{i}\,\beta\,[\![q_h]\!](x_{j+\frac{1}{2}}), \tag{2.4a}$$

$$\widehat{q}_h(x_{j+\frac{1}{2}}) = q_h^+(x_{j+\frac{1}{2}}) + \boldsymbol{i}\,\alpha\,[\![u_h]\!](x_{j+\frac{1}{2}}), \tag{2.4b}$$

where $v^-(x_{j+\frac{1}{2}})$ and $v^+(x_{j+\frac{1}{2}})$ are the left and right limits of v at $x_{j+\frac{1}{2}}$, respectively, and $[\![v]\!] = v^- - v^+$ represents the jump across the interface. We take the penalty parameters β and α to be positive constants, which makes the DG methods different from the multiscale local DG in [18]. This allows us to carry out error analysis in a way similar to [11]. Moreover, our numerical tests show that the nonzero penalty terms are necessary for reducing resonance errors.

At the two boundary points $\{a, b\}$, we define the numerical traces

$$\widehat{u}_h(a) = (1-\gamma)u_h(a) + \boldsymbol{i}\frac{\gamma}{\sqrt{f_a}}\,q_h(a) + 2\gamma, \tag{2.5a}$$

$$\widehat{q}_h(a) = \gamma q_h(a) - \boldsymbol{i}(1-\gamma)\sqrt{f_a}\,u_h(a) + 2\boldsymbol{i}\,(1-\gamma)\sqrt{f_a}, \tag{2.5b}$$

$$\widehat{u}_h(b) = (1-\gamma)u_h(b) - \boldsymbol{i}\frac{\gamma}{\sqrt{f_b}}\,q_h(b), \tag{2.5c}$$

$$\widehat{q}_h(b) = \gamma q_h(b) + \boldsymbol{i}(1-\gamma)\sqrt{f_b}\,u_h(b), \tag{2.5d}$$

where γ can be any real constant in $(0,1)$. It is easy to see that

$$\widehat{q}_h(a) + \boldsymbol{i}\sqrt{f_a}\,\widehat{u}_h(a) = 2\boldsymbol{i}\sqrt{f_a}, \quad \widehat{q}_h(b) - \boldsymbol{i}\sqrt{f_a}\,\widehat{u}_h(a) = 0,$$

which match the boundary conditions (2.2b) for the exact solutions.

2.2 The high-order multiscale approximation space

Now let us discuss our multiscale DG spaces V_h in more detail.

Our choices of multiscale DG spaces are inspired by the multiscale finite element spaces in [5, 18, 10]. In [5], Ben Abdallah and Pinaud developed a continuous finite element method using WKB basis functions that interpolate the WKB asymptotic[6] of stationary Schrödinger equation,

$$\widetilde{\varphi}(x) = \frac{A_j}{\sqrt{k(x)}} e^{\boldsymbol{i}S(x)} + \frac{B_j}{\sqrt{k(x)}} e^{-\boldsymbol{i}S(x)}, \quad x \in I_j,$$

where the wave number $k(x) = \frac{\sqrt{f(x)}}{\varepsilon}$, $S(x) = \int_{x_j}^{x} k(s)ds$, and the constants A_j and B_j are determined by the nodal values at the element boundaries.

Later, Wang and Shu in [18] developed a multiscale local DG method, the so-called WKB-LDG method, by using the "constant form" of $k(x)$ in the WKB basis functions. Their finite element space is defined as

$$E^2 = \{v_h : v_h|_{I_j} \in \text{span}\{1, e^{\boldsymbol{i}k_j(x-x_j)}, e^{-\boldsymbol{i}k_j(x-x_j)}\}, \quad j = 1, \cdots, N\},$$

where $k_j := k(x_j)$.

Recently, we developed a multiscale DG with a more compact approximation space E^1 in [10]

$$E^1 = \{v_h : v_h|_{I_j} \in \text{span}\{e^{\boldsymbol{i}k_j(x-x_j)}, e^{-\boldsymbol{i}k_j(x-x_j)}\}, j = 1, \cdots, N\}.$$

We showed that although the E^1 space is smaller than E^2, our DG method in [10] can achieve the same second order of accuracy with less resonance errors than the WKB-LDG in [18] when $h \gtrsim \varepsilon$. On very refined meshes when $h \lesssim \varepsilon$, our multiscale DG with E^1 has the second-order convergence and the WKB-LDG with E^2 has the third order.

In this paper, we consider extending the multiscale DG method in [10] to higher order approximation spaces by enriching the E^1 space with additional

basis functions. The first type of higher order spaces is obtained by including polynomial basis functions:

$$E^{p+2} = \{v_h : v_h|_{I_j} \in \text{span}\{e^{\pm \boldsymbol{i} k_j (x-x_j)}, 1, x, \cdots, x^p\}, j = 1, \cdots, N\}$$

for any $p \geq 0$.

The second type of higher order spaces is to add p additional pairs of exponential basis functions on each element:

$$T^{2p+1} = \{v_h : v_h|_{I_j} \in \text{span}\{e^{\pm \boldsymbol{i} k_j (x-x_j)}, e^{\pm 2\boldsymbol{i} k_j (x-x_j)}, \cdots, e^{\pm (p+1)\boldsymbol{i} k_j (x-x_j)}\}, \\ j = 1, \cdots, N\}$$

for any $p \geq 0$. Note that $T^1 = E^1$.

Remark 1. WKB asymptotic [6] is valid only for $f > 0$ and will break down close to turning points where $f = 0$. For our DG schemes, we require that $f(x_j)$ is not zero so that the basis functions are linearly independent. In our analysis, we assume that $f \in W^{1,\infty}(\Omega)$ and $f(x) \geq \tau > 0$. When f is negative, the solution is non-oscillatory and the analysis is easier. In implementation, we define a threshold $\tau > 0$. When $|f(x)| < \tau$, we simply replace it by τ in the basis functions. Our numerical tests show that the proposed DG schemes works for any smooth f.

3 Error estimates

In this section, we carry out error analysis for the multiscale DG methods with the finite element spaces E^{p+2} and T^{2p+1} for the model problem (2.1). We first show that the trace inequality holds for functions in these two finite element spaces. Then we prove optimal approximation orders of the L^2-projections onto these spaces when h is sufficiently small. Finally, we get the error estimates at element interfaces and in the interior of the domain by using the same energy and duality arguments as those for the multiscale DG with the E^1 space in [10].

In the rest of the paper, we use the notation $\|\cdot\|_{s,D}$ for $H^s(D)$-norm. We drop the first subindex if $s = 0$, and the second if $D = \Omega$ or Ω_h.

First we need to prove the following trace inequality for functions in our high-order multiscale finite element spaces.

Lemma 3.1. *For any function v in E^2, E^3 or T^3, T^5, and any $I_j \in \Omega_h$, when h_j is small enough, we have*

$$\|v\|_{\partial I_j} \leq C h_j^{-1/2} \|v\|_{I_j},$$

where C is a constant independent of h_j.

Proof. (i) Let us first prove the trace inequality for any function $v \in E^2$. Suppose that

$$v = \sum_{l=1}^{3} c_l \varphi_l(x) \quad \text{on } I_j = (x_{j-\frac{1}{2}}, x_{j+\frac{1}{2}}),$$

where

$$\varphi_1 = e^{\boldsymbol{i} k_j (x - x_j)}, \quad \varphi_2 = e^{-\boldsymbol{i} k_j (x - x_j)}, \quad \varphi_3 = 1.$$

Then we have

$$\|v\|^2_{\partial I_j} = \mathbf{c} A \mathbf{c}^T, \quad \text{and} \quad \|v\|^2_{I_j} = \mathbf{c} B \mathbf{c}^T,$$

where $\mathbf{c} = (c_1, c_2, c_3)$, $\mathbf{c}^T$ is the conjugate transpose of $\mathbf{c}$, and A and B are 3×3 matrices whose elements are given by

$$A_{l,m} = \varphi_l \bar{\varphi}_m(x_{j-\frac{1}{2}}) + \varphi_l \bar{\varphi}_m(x_{j+\frac{1}{2}}), \quad B_{l,m} = \int_{I_j} \varphi_l \bar{\varphi}_m \, dx, \quad l, m = 1, \cdots, 3.$$

After simple calculations, we get

$$A = 2 \begin{pmatrix} 1 & \cos 2\theta & \cos\theta \\ \cos 2\theta & 1 & \cos\theta \\ \cos\theta & \cos\theta & 1 \end{pmatrix}, \quad B = h_j \begin{pmatrix} 1 & \operatorname{sinc} 2\theta & \operatorname{sinc}\theta \\ \operatorname{sinc} 2\theta & 1 & \operatorname{sinc}\theta \\ \operatorname{sinc}\theta & \operatorname{sinc}\theta & 1 \end{pmatrix},$$

where $\theta = \frac{1}{2} k_j h_j$ and $\operatorname{sinc} x = \frac{\sin(x)}{x}$. To show that there exists a constant $r > 0$ so that $\|v\|^2_{\partial I_j} \leq r \|v\|^2_{I_j}$ for any $v \in E^2$, we consider the generalized eigenvalue problem

$$A\mathbf{c} = \lambda B \mathbf{c},$$

which can be written as

$$B^{-1} A \mathbf{c} = \lambda \mathbf{c}.$$

We can take r to be the upper bound of the eigenvalues λ. Since $\|\cdot\|_{\partial I_j}$ is a semi-norm and $\|\cdot\|_{I_j}$ is a norm on E^2 and $\{\varphi_1, \varphi_2, \varphi_3\}$ is a basis of E^2 for any $\theta > 0$, we have A is semi-positive definite and B is positive definite. Then

B^{-1} is positive definite and can be written as $B^{-1} = B^{-\frac{1}{2}}B^{-\frac{1}{2}}$, where $B^{-\frac{1}{2}}$ is a positive-definite matrix. Note that $B^{-\frac{1}{2}}AB^{-\frac{1}{2}}$ is semi-positive definite and $B^{-1}A = B^{-\frac{1}{2}}(B^{-\frac{1}{2}}AB^{-\frac{1}{2}})B^{\frac{1}{2}}$. We get that the eigenvalues of $B^{-1}A$ are all nonnegative for small $\theta > 0$. Both A and B are continuous in θ, and so are $B^{-1}A$ and its eigenvalues. After some calculations, we get that the eigenvalues of $B^{-1}A$ are bounded by $12h_j^{-1}$ as $\theta \downarrow 0$. So for $\theta > 0$ small enough, which means h_j small enough, the eigenvalues of $B^{-1}A$ satisfy $\lambda \leq Ch_j^{-1}$. This implies that

$$\|v\|_{\partial I_j}^2 \leq Ch_j^{-1}\|v\|_{I_j}^2,$$

which completes the proof for $v \in E^2$.

(ii) Next, we sketch the proof of the trace inequality for any $v \in T^3$. Using the same argument as in (i), we get

$$A = 2\begin{pmatrix} A_1 & A_2 \\ A_2 & A_3 \end{pmatrix}, \quad B = h_j\begin{pmatrix} B_1 & B_2 \\ B_2 & B_3 \end{pmatrix},$$

where

$$A_1 = \begin{pmatrix} 1 & \cos 2\theta \\ \cos 2\theta & 1 \end{pmatrix}, A_2 = \begin{pmatrix} \cos\theta & \cos 3\theta \\ \cos 3\theta & \cos\theta \end{pmatrix}, A_3 = \begin{pmatrix} 1 & \cos 4\theta \\ \cos 4\theta & 1 \end{pmatrix},$$
$$B_1 = \begin{pmatrix} 1 & \operatorname{sinc} 2\theta \\ \operatorname{sinc} 2\theta & 1 \end{pmatrix}, B_2 = \begin{pmatrix} \operatorname{sinc}\theta & \operatorname{sinc} 3\theta \\ \operatorname{sinc} 3\theta & \operatorname{sinc}\theta \end{pmatrix}, B_3 = \begin{pmatrix} 1 & \operatorname{sinc} 4\theta \\ \operatorname{sinc} 4\theta & 1 \end{pmatrix}.$$

The limits of eigenvalues of $B^{-1}A$ as $\theta \downarrow 0$ are bounded by $20h_j^{-1}$. So when h small enough, the inverse inequality holds for $v \in T^3$.

For any v in higher order E^3 and T^5 spaces, the proofs of the trace inequality are similar to that in (i). □

Next, we consider the L^2-projections onto the finite element spaces E^{p+2} and T^{2p+1}. We let $\mathbf{\Pi}_1$ be the L^2-projection onto E^{p+2} and $\mathbf{\Pi}_2$ be the L^2-projection onto T^{2p+1}. We show that the projections $\mathbf{\Pi}_1$ and $\mathbf{\Pi}_2$ have the following approximation properties.

Lemma 3.2. *For any $\varphi \in H^{s+1}(\Omega)$ and $I_j \in \Omega_h$, if h_j is small enough, we have on $E^{p+2}, p = 0, 1$*

$$\|\varphi - \mathbf{\Pi}_1\varphi\|_{I_j} \leq C\, h_j^{\min\{s,p+2\}+1}\|\varphi\|_{s+1,I_j},$$
$$\|\varphi - \mathbf{\Pi}_1\varphi\|_{\partial I_j} \leq C\, h_j^{\min\{s,p+2\}+\frac{1}{2}}\|\varphi\|_{s+1,I_j},$$

and on $T^{2p+1}, p = 1, 2$

$$\begin{aligned}\|\varphi - \mathbf{\Pi}_2\varphi\|_{I_j} \leq & C\, h_j^{\min\{s,2p+1\}+1}\|\varphi\|_{s+1,I_j},\\ \|\varphi - \mathbf{\Pi}_2\varphi\|_{\partial I_j} \leq & C\, h_j^{\min\{s,2p+1\}+\frac{1}{2}}\|\varphi\|_{s+1,I_j},\end{aligned}$$

where C *is independent of* h *but dependent on* ε*.*

Proof. We first consider the E^2 space. By Taylor expansion, we get

$$\begin{pmatrix}\varphi_1\\ \varphi_2\\ \varphi_3\end{pmatrix} = AD\begin{pmatrix}1\\ x-x_j\\ (x-x_j)^2\end{pmatrix} + \mathbf{b}\, k_j^3(x-x_j)^3 + O(k_j^4(x-x_j)^4)$$

where $\varphi_1 = e^{\boldsymbol{i}k_j(x-x_j)}, \varphi_2 = e^{-\boldsymbol{i}k_j(x-x_j)}, \varphi_3 = 1$, $D = \mathrm{diag}(1, k_j, k_j^2)$, $\mathbf{b} = (-i/6, i/6, 0)^T$, and

$$A = \begin{pmatrix}1 & i & -1/2\\ 1 & -i & -1/2\\ 1 & 0 & 0\end{pmatrix}.$$

Since $k_j \neq 0$, we have AD is invertible. Using Proposition 3.2 in [19], we immediately get that for any $u \in H^{s+1}(\Omega)$,

$$\|\mathbf{\Pi}_1 u - u\|_{I_j} \leq Ch_j^{\min\{s,2\}+1}\|u\|_{s+1,I_j}. \tag{3.1}$$

Next we estimate $\|\mathbf{\Pi}_1 u - u\|_{\partial I_j}$. By Proposition 3.1 and the proof in Proposition 3.2 in [19], there exists $v_h \in E^2|_{I_j}$ such that

$$\|v_h - u\|_{\partial I_j} \leq Ch_j^{\min\{s,2\}+1/2}\|u\|_{s+1,I_j}, \tag{3.2a}$$

$$\|v_h - u\|_{I_j} \leq Ch_j^{\min\{s,2\}+1}\|u\|_{s+1,I_j}. \tag{3.2b}$$

Using Triangle inequality and Lemma 3.1, we have

$$\begin{aligned}\|\mathbf{\Pi}_1 u - u\|_{\partial I_j} \leq & \|\mathbf{\Pi}_1 u - v_h\|_{\partial I_j} + \|v_h - u\|_{\partial I_j}\\ \leq & Ch_j^{-1/2}\|\mathbf{\Pi}_1 u - v_h\|_{I_j} + \|v_h - u\|_{\partial I_j}\\ \leq & Ch_j^{-1/2}(\|\mathbf{\Pi}_1 u - u\|_{I_j} + \|u - v_h\|_{I_j}) + \|v_h - u\|_{\partial I_j}\\ \leq & Ch_j^{\min\{s,2\}+1/2}\|u\|_{s+1,I_j}.\end{aligned}$$

The last inequality above is by (3.1) and (3.2). For the L^2-projections onto other spaces E^{p+2} and T^{2p+1}, the proofs are similar. □

Now let us state our main results. We first estimate the projections of the errors at the element interfaces.

Theorem 3.3. *Suppose (u, q) is the exact solution of the problem (2.2), and (u_h, q_h) and $(\tilde{u}_h, \tilde{q}_h)$ are the solutions of the multiscale DG methods defined by (2.3)-(2.5) on E^{p+2} with $p = 0, 1$ and T^{2p+1} with $p = 1, 2$, respectively. Assume that α and β are positive constants and $0 < \gamma < 1$. When h is small enough, we have*

$$\|[\![\mathbf{\Pi}_1 u - u_h]\!]\|_{\mathscr{E}_h} + \|[\![\mathbf{\Pi}_1 q - q_h]\!]\|_{\mathscr{E}_h} \leq C\, h^{\min\{s,p+2\}+\frac{1}{2}}(\|u\|_{s+1} + \|q\|_{s+1}),$$
$$\|[\![\mathbf{\Pi}_2 u - \tilde{u}_h]\!]\|_{\mathscr{E}_h} + \|[\![\mathbf{\Pi}_2 q - \tilde{q}_h]\!]\|_{\mathscr{E}_h} \leq C\, h^{\min\{s,2p+1\}+\frac{1}{2}}(\|u\|_{s+1} + \|q\|_{s+1}),$$

where C is independent of h.

For the projections of errors in the interior of the domain, we have the following optimal convergence result.

Theorem 3.4. *Under the assumption of Theorem 3.3, we have*

$$\|\mathbf{\Pi}_1 u - u_h\| \leq C\, h^{\min\{s,p+2\}+1}((\|u\|_{s+1} + \|q\|_{s+1}),$$
$$\|\mathbf{\Pi}_2 u - \tilde{u}_h\| \leq C\, h^{\min\{s,2p+1\}+1}((\|u\|_{s+1} + \|q\|_{s+1}),$$

where C is independent of h.

The proofs of Theorem 3.3 and Theorem 3.4 are almost the same as those of Theorem 3.3 and 3.4 for the E^1 space in [10]; the estimate of the projections of errors at element boundaries is obtained by using an energy argument and the error estimate in the interior of the domain is proved by using a duality argument. Lemma 4.4, Lemma 4.5 and Lemma 4.7 in [10] still hold for our multiscale DG methods. The only difference in the proofs is that we need to use Lemma 3.1 and Lemma 3.2 above instead of Lemma 4.3 and Theorem 3.1 in [10] for the trace inequality and the errors of the L^2-projections. To avoid repetition and redundancy, we refer the readers to [10] for details of the proofs.

Using Lemma 3.2 and Theorem 3.4 and by triangle inequality, we now have optimal error estimates for the actual errors.

Theorem 3.5. *Under the assumption of Theorem 3.3, we have*

$$\|u - u_h\| \leq C\, h^{\min\{s,p+2\}+1}((\|u\|_{s+1} + \|q\|_{s+1}),$$
$$\|u - \tilde{u}_h\| \leq C\, h^{\min\{s,2p+1\}+1}((\|u\|_{s+1} + \|q\|_{s+1}),$$

where C is independent of h.

Table 4.1: Example 4.1: L^2-errors by multiscale DG for $\varepsilon = 0.01$ and $f(x) = 10$.

N	E^1	E^2	E^3	T^3	T^5
10	6.93E-13	7.05E-13	6.38E-13	6.82E-13	6.69E-13
100	5.92E-13	5.67E-13	5.62E-13	5.74E-13	5.63E-13

4 Numerical results

In this section, we will perform several numerical tests for the proposed high-order multiscale DG methods with finite element spaces E^{p+2} and T^{2p+1}. The first example is to show the good approximation property of the multiscale finite element spaces. The basis functions in these finite element spaces approximate the solution exactly when $f(x)$ is constant. The next example is to show the convergence of the multiscale DG with these spaces for ε ranging from 0.1 to 0.001. In the last example, we apply the proposed schemes to the application of Schrödinger equation in the modeling of resonant tunneling diode (RTD).

For all the numerical tests, we use $\alpha = \beta = 1$ and $\gamma = 0.5$ for the numerical fluxes in the mutiscale DG schemes. For other positive values of α, β and $0 < \gamma < 1$, the numerical results are similar and thus we do not show them here.

4.1 Constant f

Example 4.1. In the first example, we consider the simple case with constant function $f(x)$. When $f(x)$ is a constant, the exact solution of (2.1) is in the proposed high-order finite element spaces E^{p+2} and T^{2p+1}. Thus the multiscale DG method with these spaces can compute the solution exactly with only round-off errors. The L^2-errors of the multiscale DG with E^1, E^2, E^3, T^3 and T^5 for the case $f(x) = 10$ with $\varepsilon = 0.01$ are shown in Tables 4.1. It is clear to see the round-off errors in double precision. For different values of ε, the results are similar and thus not listed here. The only noticeable difference is that numerical integration of the exponential functions may accumulate round-off errors for small ε.

4.2 Accuracy test

Example 4.2. In this example, we consider a smooth function $f(x) = \sin x + 2$. Tables 4.2, 4.3 and 4.4 list the L^2-errors and orders of accuracy by the multiscale DG scheme with different E^{p+2} spaces for $\varepsilon = 0.1, 0.01$ and 0.001 separately. And the results by spaces T^{2p+1} for different ε are listed in Tables 4.5, 4.6 and 4.7. The reference solutions are computed by polynomial-based MD-LDG P^3 method [8] with $N = 500,000$. Note that we stop refining the mesh when the errors are smaller than 10^{-8}. We can see the approximate solutions in E^{p+2} and T^{2p+1} can all achieve at least the second-order convergence when $h \gtrsim \varepsilon$ without any resonance errors. Although E^2, E^3, T^3 and T^5 can not get higher order approximations than E^1 when $h \gtrsim \varepsilon$, they do have a smaller magnitude of errors than E^1. When $h \lesssim \varepsilon$, all of them can obtain the optimal order of accuracy, i.e. E^{p+2} has a $(p+3)$th order and T^{2p+1} has a $(2p+2)$th order. In particular, we observe the 3rd order for E^2, the 4th order for E^3 and T^3, and the 6th order for T^5.

We also compare our high-order multiscale DG with the MD-LDG using polynomials for $\varepsilon = 0.01$ in Table 4.8. Standard DG methods using polynomials do not have any order of convergence until the mesh is refined to $h \lesssim \varepsilon$. For example, MD-LDG starts to converge from $N = 160$ for P^1 and $N = 80$ for P^2.

When ε becomes even smaller, a very refined mesh is needed for the standard polynomial DG to converge. There is no doubt that multiscale DG methods perform better than standard DG when $h \gtrsim \varepsilon$. Even when $h \lesssim \varepsilon$, they also approximate the solutions much more accurately than the standard DG though they all have the same convergence order. For example, when $\varepsilon = 0.01$ and $N = 80$, the error is $O(10^{-3})$ for MD-LDG using P^3 and $O(10^{-5})$ for multiscale DG using E^3 or T^3.

Overall, the proposed high-order multiscale DG methods are able to approximate the solution well when $h \gtrsim \varepsilon$ and to maintain the optimal order of convergence when $h \lesssim \varepsilon$. Thus, they are more efficient and accurate than standard DG methods for solving the stationary Schrödinger equation especially when involving different scales of ε.

4.3 Applications to Schrödinger equation

Example 4.3. In this example, we apply our proposed high-order multiscale DG methods to solve the Schrödinger equation in the simulation of the res-

Table 4.2: Example 4.2: L^2-errors and orders of accuracy by multiscale DG with E^{p+2} for $\varepsilon = 0.1$.

	E^1		E^2		E^3	
N	error	order	error	order	error	order
10	2.37E-03	–	7.76E-04	–	1.22E-04	–
20	4.42E-04	2.42	1.71E-04	2.18	5.62E-06	4.44
30	1.85E-04	2.15	6.28E-05	2.48	1.05E-06	4.13
40	1.02E-04	2.08	2.92E-05	2.67	3.28E-07	4.06
50	6.45E-05	2.05	1.57E-05	2.77	1.35E-07	3.97
60	4.45E-05	2.03	9.37E-06	2.84	6.88E-08	3.70

Table 4.3: Example 4.2: L^2-errors and orders of accuracy by multiscale DG with E^{p+2} for $\varepsilon = 0.01$.

	E^1		E^2		E^3	
N	error	order	error	order	error	order
10	2.56E-02	–	2.54E-02	–	2.22E-02	–
20	7.08E-03	1.85	3.49E-03	1.92	2.56E-03	3.12
40	2.50E-03	1.50	6.19E-04	3.44	6.28E-04	2.03
80	4.37E-04	2.52	1.22E-04	2.35	3.71E-05	4.08
160	7.17E-05	2.61	2.90E-05	2.07	1.45E-06	4.67
320	1.60E-05	2.17	5.43E-06	2.42		
640	3.89E-06	2.04	8.35E-07	2.70		

Table 4.4: Example 4.2: L^2-errors and orders of accuracy by multiscale DG with E^{p+2} for $\varepsilon = 0.001$.

	E^1		E^2		E^3	
N	error	order	error	order	error	order
10	2.47E-01	–	2.47E-01	–	2.46E-01	–
20	6.27E-02	1.98	6.27E-02	1.98	6.25E-02	1.98
40	1.58E-02	1.98	1.58E-02	1.99	1.56E-02	2.00
80	4.03E-03	1.97	3.93E-03	2.01	3.84E-03	2.02
160	1.09E-03	1.88	1.09E-03	1.85	8.47E-04	2.18
320	3.06E-04	1.83	1.37E-04	2.99	8.13E-05	3.38
640	8.52E-05	1.84	1.04E-05	3.23		

Table 4.5: Example 4.2: L^2-errors and orders of accuracy by multiscale DG with T^{2p+1} for $\varepsilon = 0.1$.

	T^3		T^5	
N	error	order	error	order
5	1.99E-03	–	4.29E-04	–
10	6.92E-05	4.84	3.92E-06	6.77
20	3.45E-06	4.33	5.46E-08	6.17
30	6.49E-07	4.12		

Table 4.6: Example 4.2: L^2-errors and orders of accuracy by multiscale DG with T^{2p+1} for $\varepsilon = 0.01$.

	T^3		T^5	
N	error	order	error	order
10	2.53E-02	–	2.52E-02	–
20	7.05E-03	1.84	7.14E-03	1.82
40	1.03E-03	2.77	2.95E-04	4.60
60	7.74E-05	6.39	1.36E-05	7.58
80	2.02E-05	4.67	1.86E-06	6.94
100	7.13E-06	4.67		

Table 4.7: Example 4.2: L^2-errors and orders of accuracy by multiscale DG with T^{2p+1} for $\varepsilon = 0.001$.

	T^3		T^5	
N	error	order	error	order
10	2.47E-01	–	2.47E-01	–
20	6.27E-02	1.98	6.27E-02	1.98
40	1.58E-02	1.99	1.58E-02	1.99
80	3.95E-03	2.00	3.94E-03	2.00
160	1.03E-03	1.94	1.03E-03	1.94
320	2.76E-04	1.90	2.17E-04	2.24
640	5.79E-06	5.57	8.79E-07	7.95

Table 4.8: Example 4.2: L^2-errors and orders of accuracy by MD-LDG with polynomials for $\varepsilon = 0.01$.

	P^1		P^2		P^3	
N	error	order	error	order	error	order
10	9.53E-01	–	9.47E-01	–	9.48E-01	–
20	9.60E-01	-0.01	9.55E-01	-0.01	1.63E+00	-0.78
40	9.51E-01	0.01	4.46E-01	1.10	7.45E-02	4.45
80	1.17E-00	-0.29	3.92E-02	3.51	4.23E-03	4.14
160	7.88E-02	3.89	4.42E-03	3.15	2.67E-04	3.98

Table 4.9: Example 4.3 : L^2-errors by multiscale DG for solving Schrödinger equation in the RTD model.

N	E^1	E^2	E^3	T^3	T^5
54	1.54E-05	5.44E-07	2.28E-07	4.63E-06	3.36E-07

onant tunneling diode (RTD) model. RTD model is used to collect the electrons which have an energy extremely close to the resonant energy. We consider the RTD model (see [5]) on the interval $[0, 135nm]$. Its conduction band profile consists of two barriers of height $-0.3v$ located at $[60, 65]$ and $[70, 75]$. A bias energy $\triangle v = 0.08$ is applied between the source and the collector regions.

The wave function of the electrons injected at $x = 0$ with an energy $E > 0$ satisfies the stationary Schrödinger equation with open boundary conditions, (1.2), with $m = 0.067m_e$. These numerical tests were also performed in [5, 18, 10].

We compute in the case of a very high energy $E = 1.11eV$ and the solution will be highly oscillating. The reference solution was obtained by the polynomial-based MD-LDG P^3 method of 13,500 cells. Figure 4.1 to 4.5 show the wave function modulus computed by the multiscale DG with 54 uniform cells with E^1, E^2, E^3, T^3 and T^5 separately. In each cell, the solution is plotted as a function using 27 points. On the right of each sets of figures is the zoomed in figure in the double barrier region. We can see although the solution is highly oscillating, all proposed schemes match the reference solution very well. In the zoomed in figures, we can see slightly oscillations in the results by E^1 (Figure 4.1) and T^3 (Figure 4.4) in $[75nm, 80nm]$. The L^2-errors are listed in Table 4.9, which shows that the higher order the space is, the smaller error the approximation has. The standard polynomial-based DG methods cannot well approximate the solution unless the mesh is very refined.

5 Concluding remarks

In this paper, we have extended the second-order multiscale discontinuous Galerkin method for one-dimensional stationary Schrödinger equations

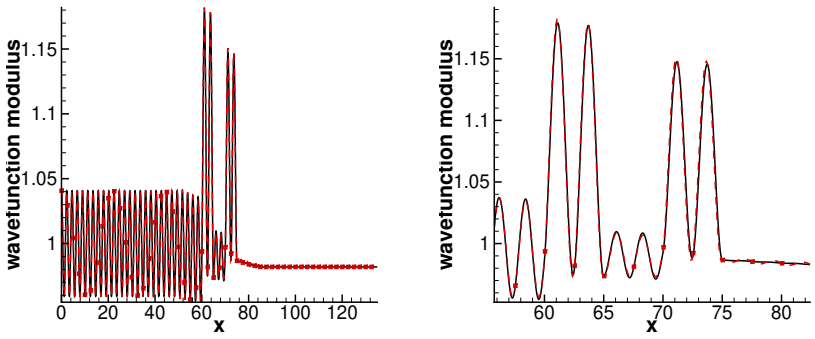

Figure 4.1: Wavefunction modulus by the multiscale DG for a high energy $E = 1.11eV$. Solid line: exact solution; dashed line: numerical solution. Left : E^1, right: zoomed in.

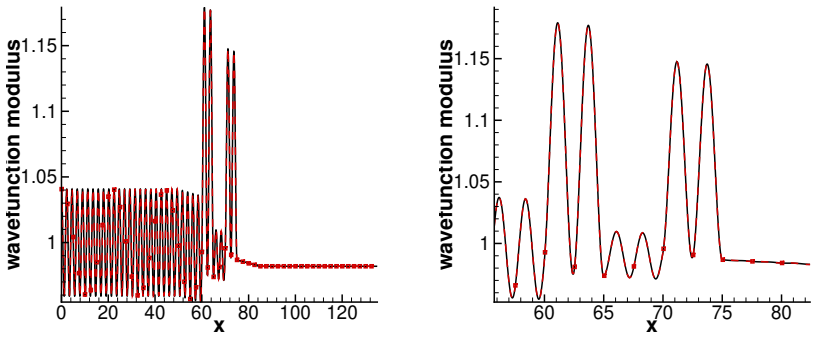

Figure 4.2: Wavefunction modulus by the multiscale DG for a high energy $E = 1.11eV$. Solid line: exact solution; dashed line: numerical solution. Left : E^2, right: zoomed in.

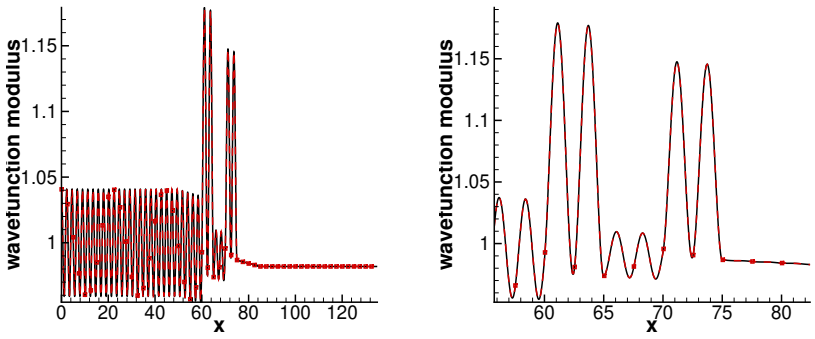

Figure 4.3: Wavefunction modulus by the multiscale DG for a high energy $E = 1.11eV$. Solid line: exact solution; dashed line: numerical solution. Left : E^3, right: zoomed in.

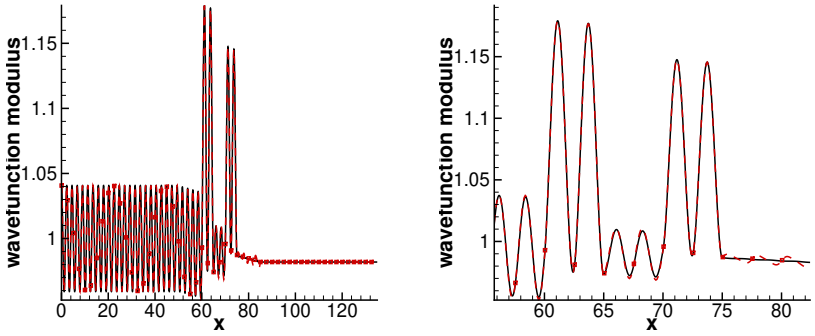

Figure 4.4: Wavefunction modulus by the multiscale DG for a high energy $E = 1.11eV$. Solid line: exact solution; dashed line: numerical solution. Left : T^3, right: zoomed in.

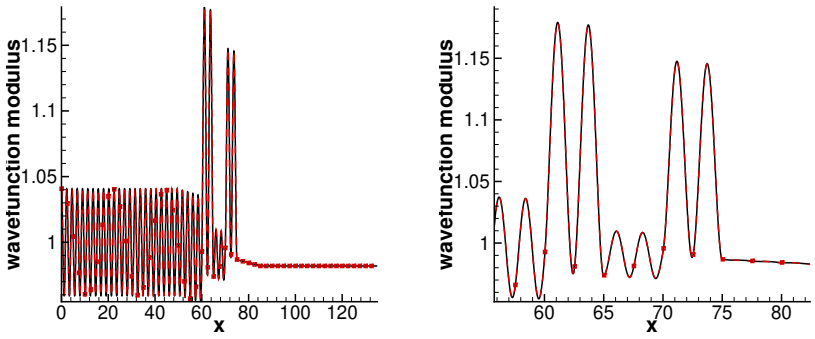

Figure 4.5: Wavefunction modulus by the multiscale DG for a high energy $E = 1.11eV$. Solid line: exact solution; dashed line: numerical solution. Left : T^5, right: zoomed in.

in our previous work to higher orders. Two types of high-order finite element spaces are proposed. The error estimates show that the high-order multiscale DG with these spaces converge optimally with respect to the mesh size h in L^2 norm when $h \lesssim \varepsilon$. Numerical experiments shows the second-order convergent rate for $h \gtrsim \varepsilon$ without any resonance errors and the optimal high-order convergence for $h \lesssim \varepsilon$. Furthermore, the schemes also demonstrate excellent accuracy on very coarse meshes when applied to Schrödinger equations. Thus, these schemes are desirable when applying to the multiscale problems with different scales of ε because they can capture the micro-scale solutions well on underresolved meshes and also can maintain high-order accuracy for macro scales. In future work, we will investigate the multiscale DG higher than second order when $h \gtrsim \varepsilon$. We would also like to generalize our multiscale DG methods to two-dimensional Schrödinger equations.

6 Acknowledgments

The authors consent to comply with all the Publication Ethical Standards. The research of the first author is supported by NSF grant DMS-1818998. The research of the second author is supported by NSF grant DMS-1418953.

References

[1] J. Aarnes and B.-O. Heimsund, *Multiscale discontinuous Galerkin methods for elliptic problems with multiple scales*, Multiscale methods in science and engineering 1–20, Lect. Notes Comput. Sci. Eng., 44. Springer, Berlin, 2005.

[2] D.N. Arnold, F. Brezzi, B. Cockburn and L.D. Marini, *Unified analysis of discontinuous Galerkin methods for elliptic problems*, SIAM J. Numer. Anal., **39**, 2002, 1749–1779.

[3] A. Arnold, N Ben Abdallah and C. Negulescu, WKB-based schemes for the oscillatory 1D Schrödinger equation in the semiclassical limit, SIAM J. Numer. Anal., 49, 2011, 1436–1460.

[4] N. Ben Abdallah, M. Mouis and C. Negulescu, *An accelerated algorithm for 2D simulations of the quantum ballistic transport in nanoscale MOSFETs*, J. Comput. Phys., **225**, 2007, 74–99.

[5] N. Ben Abdallah and O. Pinaud, *Multiscale simulation of transport in an open quantum system: Resonances and WKB interpolation*, J. Comput. Phys., **213**, 2006, 288–310.

[6] D. Bohm, *Quantum Theory*, Dover, New York, 1989.

[7] A. Buffa and P. Monk, *Error estimates for the Ultra Weak Variational Formulation of the Helmholtz equation*, ESAIM: M2AN Math. Model. Numer. Anal. **42**, 2008, 925–940.

[8] B. Cockburn and B. Dong, *An analysis of the minimal dissipation local discontinuous Galerkin method for convection-diffusion problems*, J. Sci. Comput., **32**, 2007, 233–262.

[9] B. Cockburn and C.-W. Shu, *Runge-Kutta discontinuous Galerkin methods for convection-dominated problems*, J. Sci. Comput., **16**, 2001, 173–261.

[10] B. Dong, C.-W. Shu and W. Wang, *A new multiscale discontinuous Galerkin method for the one-dimensional stationary Schrodinger equation*, J. Sci. Comput., **66**, 2016, 321–345.

[11] X. Feng and H. Wu, *Discontinuous Galerkin methods for the Helmholtz equation with large wave number*, SIAM J. Numer. Anal., **47**, 2009, 2872–2896.

[12] G. Gabard, *Discontinuous Galerkin methods with plane waves for time-harmonic problems*, J. Comput. Phys., **225**, 2007, 1961–1984.

[13] C. Gittelson, R. Hiptmair, and I. Perugia, *Plane wave discontinuous Galerkin methods: Analysis of the h-version*, ESAIM: M2AN Math. Model. Numer. Anal., **43**, 2009, 297–331.

[14] C. Negulescu, *Numerical analysis of a multiscale finite element scheme for the resolution of the stationary Schrödinger equation*, Numer. Math., **108**, 2008, 625–652.

[15] C. Negulescu, N. Ben Abdallah, E. Polizzi and M. Mouis, *Simulation schemes in 2D nanoscale MOSFETs: A WKB based method*, J. Comput. Electron., **3**, 2004, 397–400.

[16] E. Polizzi and N. Ben Abdallah, *Subband decomposition approach for the simulation of quantum electron transport in nanostructures*, J. Comput. Phys., **202**, 2005, 150–180.

[17] W. Wang, J. Guzmán and C.-W. Shu, *The multiscale discontinuous Galerkin method for solving a class of second order elliptic problems with rough coefficients*, Int. J. Numer. Anal. Model, **8**, 2011, 28–47.

[18] W. Wang and C.-W. Shu, *The WKB local discontinuous Galerkin method for the simulation of Schrödinger equation in a resonant tunneling diode*, J. Sci. Comput., **40**, 2009, 360–374.

[19] L. Yuan and C.-W. Shu, *Discontinuous Galerkin method based on non-polynomial approximation spaces*, J. Comput. Phys., **218**, 2006, 295–323.

[20] L. Yuan and C.-W. Shu, *Discontinuous Galerkin method for a class of elliptic multi-scale problems*, Int. J. Numer. Meth. Fluids, **56**, 2008, 1017–1032.

[21] Y. Zhang, W. Wang, J. Guzmán and C.-W. Shu, *Multi-scale discontinuous Galerkin method for solving elliptic problems with curvilinear unidirectional rough coefficients*, J. Sci. Comput., **61**, 2014, 42–60.